Integrating Agile Waveforms With DBF for HRWS SAR Imagery and Adaptive Jamming Suppression

GanE Dai ⬤, Sha Huan ⬤, and Lei Zhang ⬤, *Member, IEEE*

Abstract—**Range ambiguity resolving and deceptive jamming suppression are both challenges for high-resolution wide-swath SAR imagery. With the accommodation of the digital beamforming (DBF) techniques, agile waveforms are of potential to tackle the ambiguity-resolving and antijamming tasks simultaneously. In this article, an algorithm blending agile waveforms and elevation DBF is proposed for wide-swath SAR imagery and adaptive jamming suppression. A shift-stepped Costas DFC (SSC-DFC) waveform is developed with optimal shifted orthogonality. Compared with the orthogonal waveform with smeared ambiguous energy, SSC-DFC can provide precise ambiguity energy position for the spatial filter construction. Meanwhile, cyclic shifts coherence of the agile waveforms minimizes the azimuth ambiguity residual after the Doppler filtering. A serial DBF is designed for adaptive false target extraction and jammer location estimation. The jammer direction notch is only added in the false target area while executing the wide image deblurring. The subregion DBF avoids the dark strip in the final wide-swath image effectively. Extensive simulation has been presented to verify the practicability of the proposed scheme.**

Index Terms—**Agile waveform, elevation digital beamforming (DBF), high-resolution wide-swath (HRWS) SAR, jamming suppression, waveform orthogonality.**

I. INTRODUCTION

SYNTHETIC aperture radar (SAR) is an advantageous remote sensing technology that can provide high-resolution microwave image independent of weather and light conditions [1], [2], [3]. Resolution and swath width are key indicators for the SAR system application. The limitation of the range and azimuth ambiguities under the given pulse repetition frequency (PRF) drive the innovation of the wide-swath SAR system and the image processing method [4], [5]. Meanwhile, wide-swath SAR is more sustainable to the jamming influence for its extended illumination region [6], [7]. The deceptive jamming signal sent by the active jammer will form false targets in the SAR image, misleading the ground information acquisition [8].

Wide-swath imagery and deceptive jamming countermeasure seem to be two independent issues for the SAR system. Wide-swath SAR aims at resolving the range ambiguity from different subswath regions. The deceptive jamming countermeasure attempts to separate the scene echo and the jamming signal. Based on a reasonable assumption that the forwarding time of the deception jamming is greater than one pulse repetition interval (PRI) of SAR, both abovementioned issues are to distinguish the signals from the current PRI and undesired ones essentially. Therefore, waveform agility is considered to be an effective approach for both the abovementioned problems, respectively. Many research has been developed for the range ambiguity resolution based on agile waveform design. Wang [9] studied the orthogonal transmit signals based on OFDM techniques to solve the range ambiguity in SAR. A more sophisticated waveform consisting of a sequence of phased modulated chirp subpulses is proposed in [10]. Krieger [11] developed a short-term shift orthogonal (STSO) waveform. A widely accepted conclusion was drawn that the waveforms with shared spectrum cannot achieve orthogonality under arbitrary delay. So, the quasi-orthogonal waveform's performance will deteriorate when facing the distributed scene, while the STSO and OFDM only have a limited range of orthogonality. Bordoni et al. [12] suggested sending the pulses with mutually disjoint bandwidths for increased coverage, but the separated spectrum will restrict the range solution corresponding to the reduced bandwidth of a single transmitting waveform. To improve the range ambiguity suppression performance, [13] optimized the nonlinear frequency modulation (NLFM) waveform for lower cross-correlation energy (CCE). However, the cross-correlation improvement is at the price of the autocorrelation decline. A wide-swath SAR system is proposed in [14] for ship detection. A relatively small PRF is applied in this application for a wide-swath image. The ship's azimuth ambiguities are considered to be tolerated.

There are also many studies on the SAR deceptive jamming countermeasure using agile waveforms. Chirp rate perturbation and random phase modulation on linear frequency modulation (LFM) waveform were developed for SAR jamming countermeasure [15], [16]. An azimuth phase coding waveform was proposed for deceptive jamming suppression [17]. In [18], a subpulse coding scheme is developed, which uses the subpulse digital beamforming technology to suppress deceptive jamming. Some research transformed the antijamming problem into an optimization problem under the sparse assumption, it extracted the time–frequency features of the jamming signal within a dynamic synthesis aperture [19], [20]. Excavating and

enriching the spatial degree of freedom is an attractive way for the SAR jamming countermeasure. Multichannel SAR [21] and multistatic SAR [22] utilized the space–time characteristic difference between the jamming signal and the echo for the jamming suppression. Jamming cancellation methods based on dual-channel [23], there-channel [24], and multichannel [25] were proposed inspired by the displaced phase center antenna clutter suppression technology. These methods used the phase relationship between the channels to suppress the signals for the fixed jammer's location. However, the SNR loss at the dark strip is hard to overcome for the SAR imagery.

The range ambiguity resolution and azimuth coherent processing impose contradictory requirements on the agile waveform optimization in HRWS SAR, so it is hard to obtain a satisfactory wide-swath image only by waveform design. Moreover, the unique correspondence between the agile waveform and the PRI no longer exists, which is a major obstacle in distinguishing the forwarded jamming signal and the echoes from the ambiguous subswath. Although waveform agility can reduce the predictability of the transmission waveform and improve the SAR's electronic countermeasure capability to a certain extent, relying solely on the waveform agility is insufficient to address the HRWS imaging and jamming countermeasures simultaneously. Considering the elevation angle dependency of the scatter range position on the instantaneous SAR signal, integrating agile waveform with elevation DBF provides an effective solution to the abovementioned problems.

In this article, a scheme integrating agile waveforms and elevation DBF is proposed for the wide-swath SAR imagery and adaptive jamming suppression. First, a shifted stepped Costas DFC (SSC-DFC) waveform is developed based on the range ambiguity mechanism analysis for the HRSW SAR under distributed scatter scenario. This agile waveform has short-term shifted orthogonality and presents focused ambiguous energy distribution. Combined with the elevation DBF, precise positioning and suppression of the ambiguous energy can be realized. Meanwhile, the waveform coherence of the SSC-DFC greatly reduces the azimuth ambiguity residue after the image processing. Then, the space–time difference between the jamming signal and the wide-swath echo is fully utilized to identify and extract the false target area. The jammer's angle estimation is completed by the false target area with a high jamming-to-signal ratio (JSR) after the clutter cancellation. Finally, when performing the elevation DBF on the wide-swath image, the jammer's direction notch is only added in the false target region, which prevents the dark stripe near the jammer's location in the SAR image.

The contribution of this article can be summarized as follows.

1) An agile waveform integrated with DBF is developed to realize HRSW imaging. Unlike the usual optimization of low cross correlation, this waveform maximizes the coherence while maintaining the waveform diversity by short-term shifted orthogonality. This characteristic brings energy peaks to the range-ambiguous region at fixed positions, which provides an accurate location index for the elevation DBF suppression. The waveform coherence is also beneficial to improve azimuth synthesis performance.

This agile waveform combined with DBF can achieve high-quality wide-swath imaging.

2) A subregion DBF scheme joint ambiguity and jamming suppression is proposed. The spatial degree of freedom is fully exploited to realize the false target extraction and jammer direction estimation by a serial DBF. The false target pixels with high JSR are also used to indicate the areas for jamming suppression in addition to ambiguity suppression. The subarea filtering can counter deceptive jamming without the dark stripe in the SAR image.

The rest of this article is organized as follows. In Section II, the SSC-DFC waveform model is constructed, and the image performance and the orthogonality are analyzed. Section III gives the details of adaptive jamming suppression for the wide-swath SAR and the coherent SAR imaging process based on the SSC-DFC waveform. The simulation results are discussed in Section IV. Finally, Section V concludes this article.

II. SHIFTED WAVEFORM BASED ON STEPPED COSTAS DFC

A. Waveform Signal Model

This section is focused on the coding scheme for the elevation multichannel SAR system with one transmitter and N_r receivers. The transmitted signal is composed of N_a identical pulse groups $S(t)$, each of which contains N pulse denoted as $S_n(t)$. T_r is the PRI

$$S(t) = \sum_{n=1}^{N} S_n [t - (n-1) T_r], \quad n = 1, \ldots, N. \quad (1)$$

$S_n(t)$ is an SSC-DFC waveform stepped modulated by Costas arrays, which can be expressed as

$$S_n(t) = \sum_{m=1}^{M} \sum_{l=1}^{L} \text{rect} \left[\frac{t - T_{ml}}{T_s} \right] e^{j2\pi f_{nml}[t - T_{ml}]}$$

$$l = 1, \ldots, L, \quad m = 1, \ldots, M \quad (2)$$

where, $\text{rect}(\cdot)$ is the rectangular function. $T_{ml} = (m-1) LT_s + (l-1)T_s$. T_s is the width of the waveform unit with a fixed instantaneous frequency. M is equal to N, and different letters are applied here to distinguish the intrapulse and interpulse variables. Since it is a frequency modulated waveform, the waveform characteristics are determined by its frequency coding scheme f_{nml}. The frequency coding sequence of each pulse is composed of M Costas arrays. Each Costas array is of order L, and modulated by stepped subcarriers, occupying different frequency bands.

The square grids with dot marks represent the time–frequency (TF) characteristics of the SSC-DFC waveform in Fig. 1. Costas array can be regarded as L-order square grid with exactly one dot at each row and column. The key feather of the Costas array is that all the vectors formed by any two dots are distinct. So, if the square grid shift along the vertical and horizontal axis, the new array will produce only one coincidence with the original array at most [26]. This feature introduces nearly ideal ambiguity characteristics to the Costas DFC when the dot coordinates
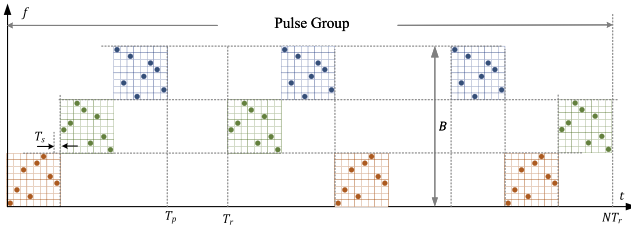
Fig. 1.   TF characteristics of the SSC-DFC waveform when $N = 3$, $L = 8$.
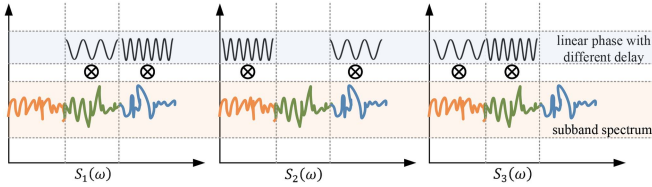

Fig. 2.   Frequency domain of each pulse in the SSC-DFC waveform. $S_1(\omega) = \mathcal{F}\{S_1(t)\}$; $S_2(\omega) = \mathcal{F}\{S_2(t)\}$; $S_3(\omega) = \mathcal{F}\{S_3(t)\}$.

are applied as the time and frequency indices of the subpulse, respectively.

Precisely, denoting the bandwidth by B, and the frequency code for the nth PRI can be expressed as

$$f_{nml} = f_{nm} + \frac{B}{ML}c_{nml} \tag{3}$$

where, c_{nml} is the frequency index of DFC in each subpulse. The subcarrier frequency in each pulse can be denoted in vector form as

$$\boldsymbol{f}_{nm} = [f_{n1}, f_{n2}, \ldots, f_{nM}] = \frac{B}{M}[1, 2, \ldots, M]\left(\boldsymbol{J}_M^n\right)^{\mathrm{T}} \tag{4}$$

where, $\boldsymbol{J}_M^n$ is the basic cyclic matrix

$$\boldsymbol{J}_M^n = \begin{pmatrix} 0 & \boldsymbol{I}_{M-n} \\ \boldsymbol{I}_n & 0 \end{pmatrix}. \tag{5}$$

The selected M DFC arrays are arranged as vectors, forming the origin coding matrix $\boldsymbol{\mathcal{C}}_n$

$$\boldsymbol{\mathcal{C}}_n = [\boldsymbol{c}_{n1}, \boldsymbol{c}_{n2}, \ldots, \boldsymbol{c}_{nM}] = \boldsymbol{\mathcal{C}}\left(\boldsymbol{J}_M^n\right)^{\mathrm{T}}. \tag{6}$$

c_{nml} is the element of matrix $\boldsymbol{\mathcal{C}}_n$ located in the mth column and lth row. It can be seen that the pulses in the group are cyclically shifted in the steps of the subpulses. The pulse contains M Costas DFCs, so M different pulses can be obtained through cyclic displacement to constitute a pulse group. It can be seen from the spectrum in Fig. 2 that the frequency spectrum of the SSC-DFC waveform is composed of N subbands of the Costas DFC. In the SSC-DFC waveform set, the time segment occupied by the same subband moves cyclically between each pulse. The time–domain shift will only add different linear phases to the frequency bands and will not change the amplitude distribution in the frequency domain.

The Costas DFC obtains the optimal sidelobe performance when its order L follows the Nyquist choice [27]. The L can be
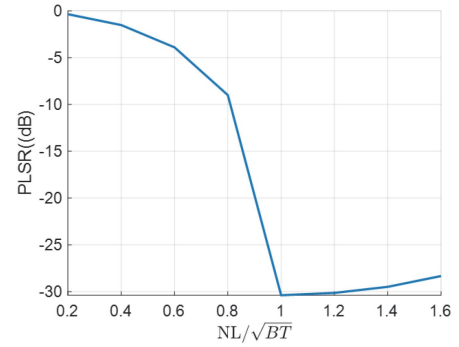

Fig. 3.   PSLR with different Costas orders under the same time–bandwidth product.

calculated by the following:

$$L = \frac{\mathrm{round}\left(\sqrt{BT_p}\right)}{N}. \tag{7}$$

Lower order will bring about an unexpected high grating lobe after the matched filter.

B. Waveform Performance Analysis

The ambiguity function (AF) is performed to reconstruct the range and Doppler profile. The AF of the pulse group is equivalent to the sum of each pulse's respective AF

$$\chi(\tau, \xi) = \sum_{n=1}^{N} \chi_n(\tau, \xi) = \sum_{n=1}^{N} \int_{-T_p}^{T_p} S_n(t) S_n^*(t - \tau) \mathrm{e}^{\mathrm{j}2\pi\xi t} dt. \tag{8}$$

For the SSC-DFC waveform, attributed to the permutation property of the Costas array, the frequency differences between all the subpulse pairs are different. So, the AF of the SSC-DFC displays an approximate ideal thumbtack at the origin. But if the waveform subbands are modulated by the same Costas array, the Doppler delay coupling peak will appear at the integer multiple of LT_s. Using different Costas arrays can not only improve the waveform agility but also suppress the Doppler delay coupling. It can be seen from the AF diagram in Fig. 4 that the frequency–delay coupling can be reduced from 3.52 to 16.72 dB with different Costas arrays in each subbands.

C. Jamming Suppression Discussion

The deceptive jamming signal reaches the SAR receiver lagging the echoes from the jammer's position. Therefore, the false target generated by the deceptive jamming will appear at a farther position from the jammer. The range between the false target and the jammer is determined by the forwarding delay. The false target will no longer follow the dependency of the angle of arrival (AoA) and the delay time from the real scatter, so the elevation DBF can realize the jammer suppression by spatial filtering based on the precise estimation of the jammer location. Moreover, the Doppler sensitivity of the SSC-DFC waveform can counter the frequency–shift interference [28].
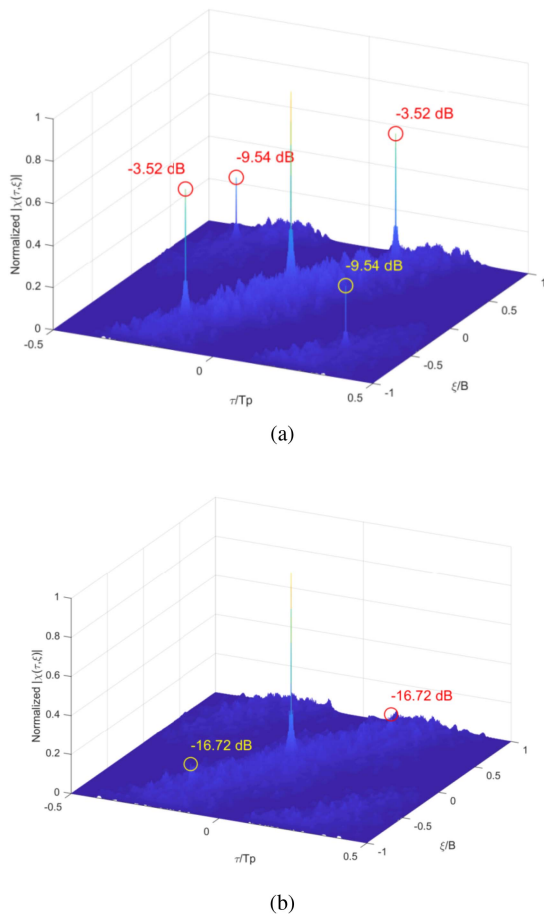
Fig. 4. AF of the SSC-DFC waveform. (a) SSC-DFC with the same Costas array on each subband. (b) SSC-DFC with different Costas arrays on each subband.

Fig. 5. Match and mismatch comparison for point and line targets. (a) Up–down chirp waveform with a point target. (b) Up–down chirp waveform with a line target (T_p length). (c) Costas DFC waveform with a point target. (d) Costas DFC waveform with a line target (T_p length). (e) Ratio of the cross correlation to the autocorrelation with various line target length. "corr" represents autocorrelation, "xorr" represents cross correlation for simplicity.

D. Orthogonality Analysis

To realize the HRSW imaging, an ideal approach is using the orthogonal processing between the PRIs to resolve the range ambiguity. In the academic scenario, when the radar target only consists of one or a few closely spaced scatters, the conventional quasi-orthogonal waveform can solve the range ambiguity across the subswath defined by PRI. Quasi-orthogonal waveforms with common spectral support will have a peak after the matched filter, and output smeared energy after the mismatched for a point scatter. However, for an extended scene filled with a large number of distributed scatters, the smeared energy will accumulate due to the energy from all these scattering points. When the range of the distributed scene is equal to the corresponding range to the pulse width, even if the cross-correlation level is very low, the mismatched output will raise to a comparable level to the matched output, leading to a loss of orthogonality.

Fig. 5 demonstrates the range compression of two quasi-orthogonal waveforms under the point and line targets, respectively. Fig. 5(e) shows the cross-correlation performance comparison of two quasi-orthogonal waveforms with shared spectrum when facing distributed targets with different lengths. The cross correlations of the tw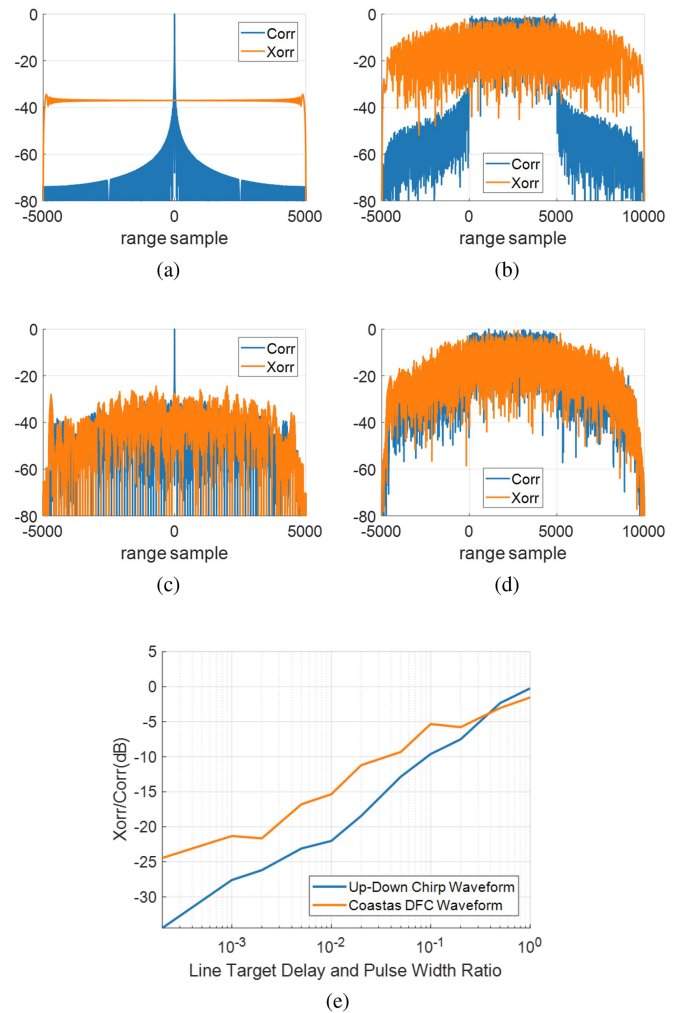o quasi-orthogonal waveforms both deteriorate as the range coverage of distributed targets increases. The orthogonality merit diminishes as the line target increases to the equivalent length of the pulse width. The magnitude of the mismatched signal is comparable to that of the matched signal. The quasi-orthogonality of the waveforms brings little contribution to the range ambiguity resolution.

The mismatched output is related to the CCE of these waveforms [13]. The CCE is defined as

$$\text{CCE} = \int |S_1(\omega)|^2 \cdot |S_2(\omega)|^2 d\omega. \tag{9}$$

The ideal orthogonal condition is the segmentation in the frequency domain, that is, orthogonal waveforms occupy nonoverlapping spectral distributions [29]. If the orthogonal waveforms require common spectrum support without loss of resolution, the waveform optimization trend based on CCE is to introduce fluctuation to the waveform amplitude in the frequency domain. Staggered amplitude fluctuations will reduce the CCE

and suppress the mismatch energy from the distributed scatters. However, the amplitude fluctuation in the frequency domain will lead to the autocorrelation performance degradation of the waveform. The signal energy will disperse from the peak to the side lobe. Even if there is a constraint on PSLR, the deterioration of ISLR will lead to the degradation of the imaging quality in the range profile. Moreover, the sidelobe diversity of different waveforms leads to azimuth synthesis difficulty, resulting in a further decline in the imaging quality.

As analyzed previously, there are contradictions between autocorrelation and cross-correlation optimization facing the extended scattering scenarios. Only the waveform design cannot be an effective approach to solve the ambiguity of the wide swath SAR imaging. Considering that the ambiguity position does not follow the dependency of the AoA, the elevation DBF can also be used to suppress the range ambiguity as well as the jamming signal.

The elevation DBF is applied as a spatial filter to retain the echo from the range cell and suppress the ambiguity energy. The unambiguous output of the traditional quasi-orthogonal waveform is focused, so the DBF spatial filtering requires a narrow beam to reduce sidelobe interference from the nearby scatter points. While the signal energy at the ambiguous locations is smeared along the range of cT_p length, complete suppression of ambiguous energy requires a wide coverage of the beam notch. This is a contradictory requirement for the elevation DBF.

Therefore, this article refers to the STSO waveform idea and proposes the SSC-DFC waveform. Costas DFC is applied as the subband waveform. N SSC-DFC waveforms can be constructed by the subband modulation and the cyclic shift. Within the range of T_p/N, the waveforms can achieve ideal orthogonality due to the spectrum segmentation. The range ambiguity will focus on the integer multiple positions of T_p/N, which is convenient for the notch setting in the spatial filtering. The different waveforms in the pulse group are constructed by cyclic shift, so their spectrum amplitudes are consistent. When performing the azimuth synthesis, the different waveforms are completely coherent. So, azimuth ambiguity suppression can achieve good performance when synthesizing the echo group images. Compared with the fixed waveform that only relies on the elevation DBF, the SSC-DFC waveform is more agile. Due to the separation of the ambiguous energy, the focused ambiguous peak declines, which can also reduce the requirement for DBF. It can be seen from Fig. 6 that the ambiguous peaks are reduced by 3.52 and 9.54 dB, respectively, after the dispersion.

Therefore, the wide swath SAR countermeasure imaging can be addressed by the combination of the waveform design and the elevation DBF. It should be noted that the numbers of the jammers and the range ambiguity share the spatial degree of freedom of the elevation DBF.

III. ELEVATION MULTICHANNEL SAR JOINT JAMMING SUPPRESSION AND WIDE-SWATH IMAGE

A. Elevation Multichannel Imaging Geometry

As shown in Fig. 7, a side-looking imaging geometry is applied in this article for the SSC-DFC SAR in the jamming
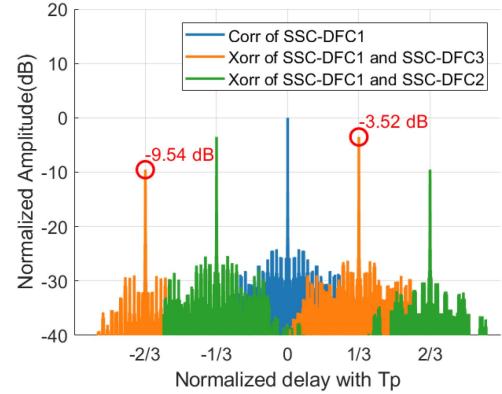

Fig. 6. Autocorrelation and cross correlation of different SSC-DFC waveforms in the pulse group.
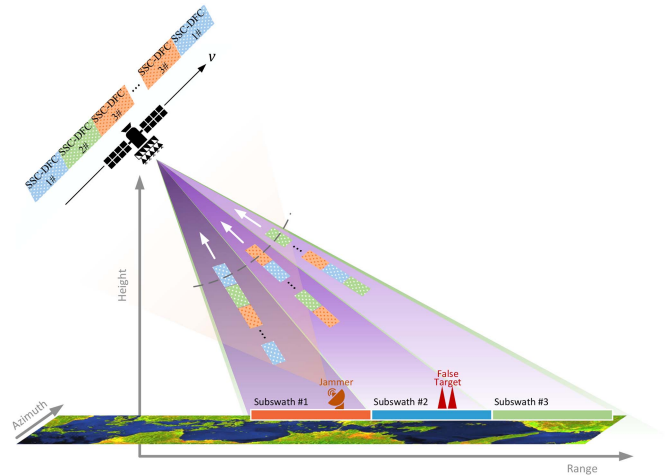

Fig. 7. SSC-DFC SAR imaging geometry in the jamming scenario.

scenario. The antenna phase center (APC) of radar moves along the solid line at a constant velocity of v. The flight path of APC forms the synthetic aperture in the azimuth domain taking the midpoint at $t_a = 0$. The range direction is line perpendicular to the azimuth direction. There are N subswaths along the range. The slant distance difference between both ends of each subswath is $R_r = T_r c/2$, c is the speed of light. K receive antennas are placed perpendicular to the APC path for the elevation DBF. The tilt of the antenna is set so that the normal axis points to the elevation angular center of the wide-swath scene. The channel spacing is denoted by d, and the transmitting channel is located at the center of the antenna aperture. The jammer in the scenario intercepts and retransmits the radar signal. The interference signals can form false targets at further distances due to the forwarding delay. A simple reference surface with constant topographic height is adopted in this article, so the direction of arrival (DoA) mismatch problem will not occur. This assumption allows for the achievable performance comparison of the simulation.

Without loss of generality, Fig. 7 shows the transmitting waveform sequence and the echo sequence from the different

subswaths when $N = 3$. The antenna sends each SSC-DFC waveform sequentially according to the PRI. Due to the difference in delay, the SSC-DFC waveforms from different PRI are reflected by different subswaths and will be received by the antenna at the same time. The received signals from all the receiving channels in each PRI will be used for wide-swath imaging and anti-interference processing.

B. Imaging Processing

The imaging processing is executed in a polar coordinate system. $\tau_{c,i}(n, n_a)$ is the echo delay history of the ith subswath center $(r_{c,i}, 0)$ during the APC movement. It can be expressed as

$$\tau_{c,i}(n, n_a) = \frac{2R_{c,i}(n, n_a)}{c} \quad (10)$$

where, $R_{c,i}(n, n_a)$ is the polar radius history between the transmitter to the ith subswath center

$$R_{c,i}(n, n_a) = \sqrt{r_{c,i}^2 + \{[(n-1) + (n_a - 1)N]T_r v\}^2} \quad (11)$$

where, $r_{c,i}$ denotes the radius coordinate of the ith subswath center.

Similarly, the coordinates of the scattering points in each subswath are represented by $(r_{t,i}, \theta_{t,i})$. $\tau_{t,i}(n, n_a)$ denotes the echo delay of the scatting point of the ith subswath. $R_{t,i}(n, n_a)$ represents the instantaneous ranges between the APC and the scattering point $(r_{t,i}, \theta_{t,i})$

$$\tau_{t,i}(n, n_a) = \frac{2R_{t,i}(n, n_a)}{c} \quad (12)$$

$$R_{t,i}(n, n_a) =$$

$$\sqrt{r_{t,i}^2 \cos^2 \theta_{t,i} + \{[(n-1) + (n_a - 1)N]T_r v - r_{t,i} \sin \theta_{t,i}\}^2}. \quad (13)$$

The jamming signal delay depends on the jammer location (r_J, θ_J) and the forwarding delay τ_j

$$\tau_J(n, n_a) = \frac{2R_J(n, n_a)}{c} + \tau_j. \quad (14)$$

Under the assumption that the SAR system is narrowband, the received signal at the kth elevation channel in the baseband can be expressed as the following:

$$y_k(t; n, n_a) = \sum_{i=1}^{N} \sigma_{t,i} \cdot e^{-j2\pi f_c \tau_{t,i}(n, n_a)}$$

$$\cdot \alpha_k(\phi_{t,i}) \cdot s_n[t - \tau_{t,i}(n, n_a)]$$

$$+ A_J \cdot e^{-j2\pi f_c \tau_J(n, n_a)}$$

$$\cdot \alpha_k(\phi_J) \cdot s_n[t - \tau_J(n, n_a)] + n_k(t) \quad (15)$$

where

$$\alpha_k(\phi) = e^{-\frac{j2\pi k d \sin(\phi)}{\lambda}}, \quad k = 0, 1, \dots, K - 1. \quad (16)$$

$\sigma_{t,i}$ is the radar cross-section of the target point on the located subswath and the ambiguous positions on the other subswaths, A_J is the jammer gain, f_c is the carrier frequency, $\phi_{t,i}$ and ϕ_J are the elevation angles of the target and the jammer respectively, and $n_k(t)$ is additive white noise generated by the receiver in the kth elevation channel.

Consider the waveform structure shown in Fig. 1 and the subswath division in Fig. 7 in which $N = M = 3$, the echo sequence is divided into three echo groups. The SSC-DFC waveforms and the reflected subswaths have a fixed correspondence in each group. The image process is executed on each echo group.

First, frequency–domain matched filtering is used for the deramp processing. The deramp processing is performed according to the region center of each subswath. The reference signal $Ref_i(n, n_a)$ used for each subswath obeys the fixed correspondence of the current echo group. The following descriptions uses the 1st echo group as an example. The expression of the reference signal can be written as

$$Ref_1(t; 1, n_a) = e^{-j2\pi f_c \tau_{c,1}(1, n_a)} s_1(t - \tau_{c,1}(1, n_a))$$

$$Ref_2(t; 1, n_a) = e^{-j2\pi f_c \tau_{c,2}(1, n_a)} s_3(t - \tau_{c,2}(1, n_a))$$

$$Ref_3(t; 1, n_a) = e^{-j2\pi f_c \tau_{c,3}(1, n_a)} s_2(t - \tau_{c,3}(1, n_a)). \quad (17)$$

The frequency domain product of the echo pulse and the conjugate of the reference signal is the deramped signal without the residual video phase. Here, we consider both the target scatter point and the corresponding scatter points located at the ambiguous position $(r_{t,i'}, \theta_{t,i})$ in the other subswath. $r_{t,i'} = r_{t,i} \pm p\frac{cT_r}{2}$ $(p \in \mathbb{Z})$. The jammer may intercept the waveform and forward it in the following PRIs, and $S_J(\omega)$ represents the SSC-DFC waveform spectrum of the jamming signal in the current echo group. The deramped signal with $Ref_1(t; 1, n_a)$ can be derived as

$$F_{\text{deramp},1k}(\omega; 1, n_a)$$

$$= \sigma_{t,1}|S_1(\omega)|^2 \alpha_k(\phi_{t,1}) e^{-j\frac{2(\omega_c + \omega)}{c}[R_{t,1}(1, n_a) - R_{c,1}(1, n_a)]}$$

$$+ \sigma_{t,2}S_3(\omega)S_1^*(\omega)\alpha_k(\phi_{t,2}) e^{-j\frac{2(\omega_c + \omega)}{c}[R_{t,2}(1, n_a) - R_{c,1}(1, n_a)]}$$

$$+ \sigma_{t,3}S_2(\omega)S_1^*(\omega)\alpha_k(\phi_{t,3}) e^{-j\frac{2(\omega_c + \omega)}{c}[R_{t,3}(1, n_a) - R_{c,1}(1, n_a)]}$$

$$+ A_J S_J(\omega)S_1^*(\omega)\alpha_k(\phi_J) e^{-j\frac{2(\omega_c + \omega)}{c}[R_J(1, n_a) + \frac{c\tau_j}{2} - R_{C,1}(1, n_a)]} \quad (18)$$

where, $\omega_c = 2\pi f_c$.

The first-order Taylor expansion about the slow time is applied for the approximation of the historical slant range difference

$$R_{t,i}(n, n_a) - R_{c,i'}(n, n_a)$$

$$\approx r_{t,i} - r_{c,i'} - \sin(\theta_{t,i})[(n-1) + (n_a - 1)N]T_r v. \quad (19)$$

Keystone resampling can be applied here to decouple the radius and the azimuth by slow-time interpolation. It can also calibrate the radius migration between the pulses

$$t_{n,n_a} = \frac{(\omega_c + \omega)[(n-1) + (n_a - 1)N]T_r}{\omega_c}. \quad (20)$$

The instantaneous frequency ω is ranging from $-1/2T_r$ to $1/2T_r$. So the resampled signal can be expressed as follows:

$$
\begin{aligned}
&F_{ra,1k}\left(\omega;1,n_a\right) \\
&= \Big[\sigma_{t,1}\left|S_1(\omega)\right|^2\alpha_k\left(\phi_{t,1}\right)e^{-j\frac{2\omega_c\left(r_{t,1}-r_{c,1}\right)}{c}} \\
&\quad + \sigma_{t,2}S_3(\omega)S_1^*(\omega)\alpha_k\left(\phi_{t,2}\right)e^{-j\frac{2\omega_c\left(r_{t,2}-r_{c,1}\right)}{c}} \\
&\quad + \sigma_{t,3}S_2(\omega)S_1^*(\omega)\alpha_k\left(\phi_{t,3}\right)e^{-j\frac{2\omega_c\left(r_{t,3}-r_{c,1}\right)}{c}}\Big] \\
&\quad \times e^{-j\frac{2}{c}\left[\omega(r_{t,1}-r_{c,1})-\omega_c v\sin(\theta_{t,i})t_{1,n_a}\right]} \\
&\quad + A_J S_J(\omega)S_1^*(\omega)\alpha_k\left(\phi_J\right)\times e^{-j\frac{2\omega_c\left(r_J+\frac{c\tau_j}{2}-r_{c,1}\right)}{c}} \\
&\quad \times e^{-j\frac{2}{c}\left[\omega\left(r_J+\frac{c\tau_j}{2}-r_{c,1}\right)-\omega_c v\sin(\theta_{t,i})t_{1,n_a}\right]}.
\end{aligned} \tag{21}
$$

The radius compression can be obtained by an inverse Fourier operation in the frequency domain. The focused signal can be written as

$$
\begin{aligned}
&S_{rt,1k}\left(t;1,n_a\right) \\
&= \sigma_{t,1}\chi_{11}\left[t-\frac{2\left(r_{t,1}-r_{c,1}\right)}{c}\right] \\
&\quad \cdot \alpha_k\left(\phi_{t,1}\right)e^{-j\frac{2\omega_c}{c}\left[\left(R_{t,1}(1,n_a)-R_{c,1}(1,n_a)\right)\right]} \\
&\quad + \sigma_{t,2}\chi_{13}\left[t-\frac{2\left(r_{t,1}-r_{c,1}\right)}{c}\right] \\
&\quad \cdot \alpha_k\left(\phi_{t,2}\right)e^{-j\frac{2\omega_c}{c}\left[R_{t,2}(1,n_a)-R_{c,1}(1,n_a)\right]} \\
&\quad + \sigma_{t,3}\chi_{12}\left[t-\frac{2\left(r_{t,1}-r_{c,1}\right)}{c}\right] \\
&\quad \cdot \alpha_k\left(\phi_{t,3}\right)e^{-j\frac{2\omega_c}{c}\left[R_{t,3}(1,n_a)-R_{c,1}(1,n_a)\right]} \\
&\quad + A_J\chi_{J1}\left[t-\frac{2\left(r_J-r_{c,1}\right)}{c}\right] \\
&\quad \cdot \alpha_k\left(\phi_J\right)e^{-j\frac{2\omega_c}{c}\left[R_J(1,n_a)+\frac{c\tau_j}{2}-R_{c,1}(1,n_a)\right]}
\end{aligned} \tag{22}
$$

where, $\chi_{ij}(t)$ denotes the cross-correlation function of the ith and jth SSC-DFC. For precise angle focusing, the history of the slant range is expanded at $\theta_{t,i}=0$ by the following:

$$
\begin{aligned}
&R_{t,i}\left(n,n_a\right)-R_{c,i'}\left(n,n_a\right) \\
&\approx \hat{R}_{t,i}\left(n,n_a\right)-R_{c,i'}\left(n,n_a\right)-\frac{r_{t,i}vt_{1,n_a}}{\hat{R}_{t,i}\left(n,n_a\right)}\theta_{t,i}
\end{aligned} \tag{23}
$$

where, $\hat{R}_{t,i}(n,n_a)$ is the historical slant range of $(r_{t,i},\theta)$. It has been proved that when $\theta_{t,i}$ is relatively small in the spotlight mode, the higher order terms have little effect on the imaging performance [30]. Radius focusing enables the phase compensation and the angle interpolation along each radius cell

$$
\mathcal{P}_i\left(n,n_a\right)=\delta\left[t-\frac{2\left(r_{t,1}-r_{c,1}\right)}{c}\right]e^{-j\frac{2\omega_c}{c}\left[\hat{R}_{t,i}(n,n_a)-R_{c,i'}(n,n_a)\right]} \tag{24}
$$

where, $\delta(t)$ is the impulse function

$$
t'_{1,n_a} = \frac{r_{t,i}t_{1,n_a}}{\hat{R}_{t,i}\left(n,n_a\right)}. \tag{25}
$$

Finally, the angle compression can be obtained by the slow time DFT, then the targets, the ambiguous targets, and the false targets will focus on separated parts on the polar coordinate plane.

Through the processing previously, each echo group generates N images with a width comparable to that of the PRI. These narrow images need to be spatial filtered by the elevation DBF for range ambiguity suppression before they can be rearranged into a wide-swath image.

C. Jammer Location Under HRSW SAR

For each range cell in the narrow image, the focused energy not only comes from the scatter located at this cell, but also from $2(N-1)$ ambiguous range cells from the other subswaths. There also will be jamming signals from the jammer's DoA at the cells with the false target. The relative differences between the target range cell and the ambitious source cells are fixed, and they are determined by the pulse waveform structure in the pulse group. For the SSC-DFC waveform shown in Fig. 1, the four ambiguous sources of the range cell $r_{t,i}$ are $r_{ta,i,1l},r_{ta,i,1r}$, $r_{ta,i,2l}$, and $r_{ta,i,2r}$ respectively

$$
\begin{aligned}
r_{ta,i,1l} &= r_{t,i}+\left[1-\left\lfloor\frac{i+1}{3}\right\rfloor 3\right]R_r-\frac{c}{2}\frac{T_p}{3} \\
r_{ta,i,1r} &= r_{t,i}+\left[1-\left\lfloor\frac{i+1}{3}\right\rfloor 3\right]R_r+\frac{c}{2}\frac{2T_p}{3} \\
r_{ta,i,2l} &= r_{t,i}+\left[2-\left\lfloor\frac{i+2}{3}\right\rfloor 3\right]R_r-\frac{c}{2}\frac{2T_p}{3} \\
r_{ta,i,2r} &= r_{t,i}+\left[2-\left\lfloor\frac{i+2}{3}\right\rfloor 3\right]R_r+\frac{c}{2}\frac{T_p}{3}
\end{aligned} \tag{26}
$$

where, $\lfloor\cdot\rfloor$ indicates the rounding down operation. R_r is the subswath width.

The elevation angle of each ambiguous source can be calculated as follows:

$$
\sin(\phi) = \frac{H}{r} \approx \sin\left(\phi_{t,i}\right)\left(1-\frac{\Delta r}{r_{t,i}}\right) \tag{27}
$$

where, Δr is the range of the ambiguous source from $r_{t,i}$.

Considering the overlapping echoes from multiple subswaths, a serial DBF is applied here for adaptive false target extraction and jammer location estimation. First, $N_s(N_s\geq 2N)$ channels are sequentially chosen from the elevation array to from $K-N_s+1$ channel groups by a sliding window. The sliding step is 1. Each channel group uses the orthogonal projection matrix related to each range cell for clutter suppression, which will improve the JSR. When $N=3$, the steering vector of the range cell $r_{t,i}$ and four steering vectors of the ambiguous source cells are combined to form a matrix $U_{t,i}$. The length of the steering vector in $U_{t,i}$ is equal to the element number in each array group,

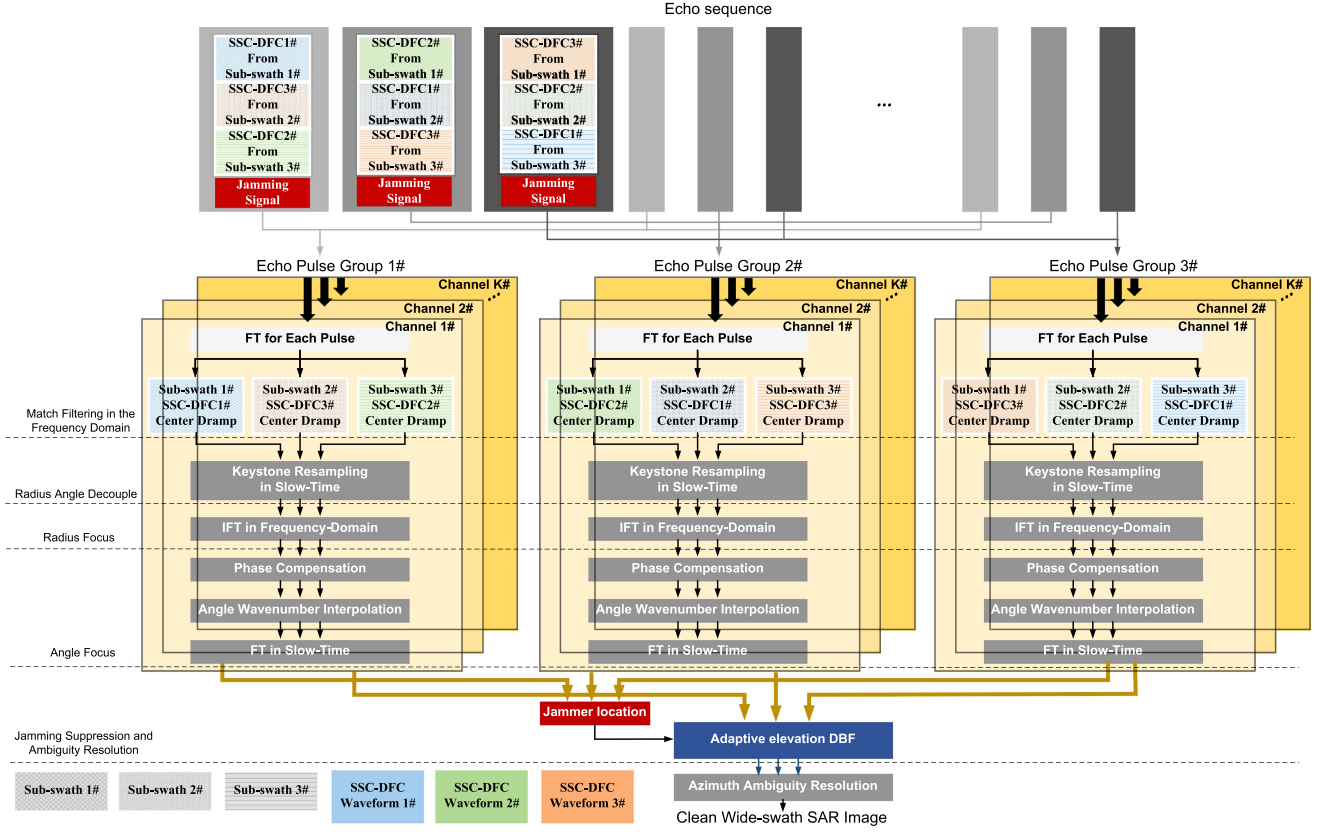Fig. 8. Flow chart of the antijamming wide-swath SAR imaging.

which is N_s

$$U_{t,i} = [v_{t,i}, v_{ta,i,1l}, v_{ta,i,1r}, v_{ta,i,2l}, v_{ta,i,2r}]. \qquad (28)$$

The orthogonal projection matrix P is constructed as follows [31]:

$$P_{t,i} = I - U_{t,i} \left(U_{t,i}{}^{H} U_{t,i} \right)^{-1} U_{t,i}{}^{H}. \qquad (29)$$

The orthogonal projection weight vector of the elevation spatial filter at this stage is

$$w_{t,i} = c_q^{T} P_{t,i}. \qquad (30)$$

where, c_q is the constraint value vector which has only one nonzero vector 1 at the qth element. The clutter cancellation result can be obtained by multiplying $w_{t,i}$ according to the range position r_{ti} of the focused images. An appropriate threshold can be set to get the false target area. Only the signals from the jammer's DoA exist in this area. After the first stage of DBF, the jammer location problem can be converted into a DoA estimation problem with a single source. The remaining $K - N_s + 1$ degrees of freedom (DoF) can be utilized by a traditional spectral estimation algorithm for the jammer DoA ϕ_J. All the pixels in the false target area can be used for the jammer location to improve the estimation accuracy. As shown in Fig. 9, false target identification and jammer location are realized by the space DoF within and between the array groups.
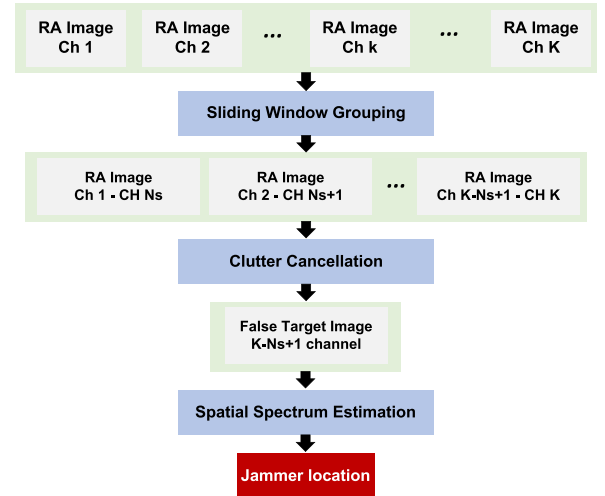

Fig. 9. Flowchart of the jammer location.

D. Spatial Filtering for Range Ambiguity Resolving and Jamming Suppression

After obtaining the precise DoA of the jammer, all the elevation DoF can be applied for range ambiguity resolving and jamming suppression by a subregion DBF. Different methods are used for spatial filtering in areas with and without false targets. In the false target area, the main beam of the array pattern points to
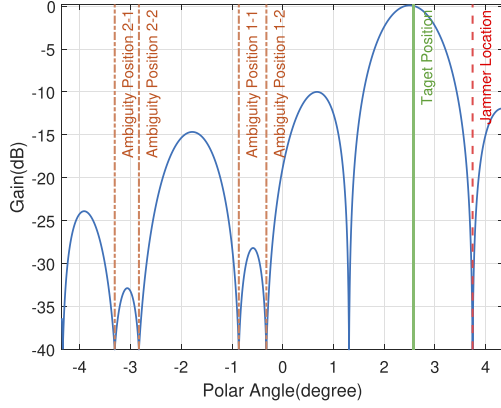
Fig. 10. Array pattern of the elevation DBF with $\boldsymbol{w}_{J,i}$.

the range cell r_{ti}, and notches are placed toward the ambiguous source cells and the jammer location. The DBF weight vector is calculated as follows:

$$\boldsymbol{w}_{J,i} = \left[\boldsymbol{U}\boldsymbol{J}_{t,i}(\boldsymbol{U}\boldsymbol{J}_{t,i})^{\mathrm{H}} \right]^{-1} \boldsymbol{U}\boldsymbol{J}_{t,i}\boldsymbol{c_1} \qquad (31)$$

where, $\boldsymbol{U}\boldsymbol{J}_{t,i} = [\boldsymbol{U}_{t,i}, \ \boldsymbol{v}_j]$ is the constraint matrix.

As shown in Fig. 10, the array pattern of the elevation DBF points to the target marked by the solid line, and it forms four notches at the ambiguous range angle and one notch at the jammer angle, marked by the orange dotted lines and red dashed line separately.

$\boldsymbol{w}_i$ is applied for the ambiguity resolution in the jamming-free image zone

$$\boldsymbol{w}_i = \left(\boldsymbol{U}_{t,i}\boldsymbol{U}_{t,i}{}^{H} \right)^{-1} \boldsymbol{U}_{t,i}\boldsymbol{c_1}. \qquad (32)$$

So, the subarea DBF realizes the unambiguous anti-interference image in the wide swath scene, it can preserve the image information near the jammer's position without a dark stripe in the SAR image.

E. Azimuth Doppler Filtering

Finally, the azimuth angle ambiguity introduced by then the N echo groups decimation needs to be addressed. For the θ_qth ambiguity number introduced by the echo group decimation, the angular Doppler steering vectors on the θ_lth azimuth grid with θ_qth ambiguity number can be expressed as

$$\boldsymbol{\alpha}_{(\theta_l,\theta_q)} = \left[e^{j2\pi\left(f_{\theta_l} + \frac{(\theta_q-1)f_e}{N}\right)\frac{t'_{1,na}}{N}}, e^{j2\pi\left(f_{\theta_l} + \frac{(\theta_q-1)f_e}{N}\right)\frac{t'_{2,na}}{N}}, \ldots, \right.$$
$$\left. e^{j2\pi\left(f_{\theta_l} + \frac{(\theta_q-1)f_e}{N}\right)\frac{t'_{n,na}}{N}}, e^{j2\pi\left(f_{\theta_l} + \frac{(\theta_q-1)f_e}{N}\right)\frac{t'_{N,na}}{N}} \right]^{\mathrm{T}} \qquad (33)$$

where, f_{θ_l} is the angular Doppler on the θ_lth azimuth grid, f_e is the angle sampling frequency after the interpolation. These steering vectors form the matrix $\boldsymbol{A}_{\theta_l} = [\boldsymbol{\alpha}_{\theta_l,1}, \ldots, \boldsymbol{\alpha}_{\theta_l,\theta_q}, \ldots, \boldsymbol{\alpha}_{\theta_l,N}]$. Same angle line from each echo group image are arranged to form a matrix $\boldsymbol{S}_{r,\theta_l}$. The azimuth wide HRSW image can be reconstructed after the azimuth

TABLE I
SIMULATION PARAMETER

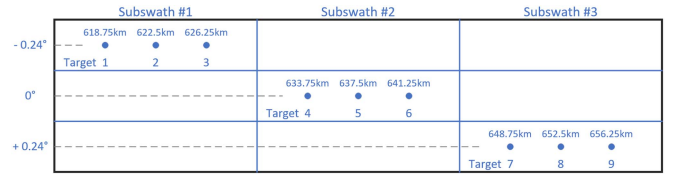| Parameter	Value
Carrier frequency (f_c)	16 GHz
Pulse width (T_p)	19.2 us
Bandwidth (B)	120 MHz
N	3
M	3
L	16
PRF ($1/T_r$)	10 KHz
Height (H)	576 Km
Velocity (v)	7571.4 m/s
Number of the channel	8
Elevation steering range	69.49° 60.78°
Antenna bore-sight direction	65.13°
Swath width	45 km
Element spacing in elevation	six wavelengths
Jammer range location	617.5Km

Fig. 11. Schematic diagram of point target imaging scene.

Doppler filtering processing as follows:

$$\overline{\boldsymbol{s}}_{r,\theta_l} = \boldsymbol{S}_{r,\theta_l} \left(\boldsymbol{A}_{\boldsymbol{\theta_l}}{}^{\mathrm{T}} \right)^{-1} \boldsymbol{c}_{\theta_q}. \qquad (34)$$

The proposed image processing flowchart is illustrated in Fig. 8.

IV. PERFORMANCE ANALYSIS

Simulations are executed to evaluate the HRSW image and antijamming performance with the proposed SSC-DFC waveform and DBF integration. The radar parameters are listed in Table I.

Among the eight receiving channels, groups of six channels are used for the clutter cancellation, and three channels are used for the jammer position estimation.

A. Point Target

First, noise-free multipoint simulations are designed for the targets at some typical locations. As shown in Fig. 11, the nine points, namely 1–9, are divided into three groups to characterize the image performance of the proposed agile waveform and DBF integration in different imaging regions. The imaging results of these point targets are given in Fig. 12.

The final imaging scene is divided into nine subregions according to the radius and azimuth ambiguity. The 1, 5, and 9 points belong to three different subregions. Meanwhile, these three points are set in various places in their subregions. Therefore, the imaging results of these three points are representative of the performance analysis of the whole scene. The focusing contour maps of points 1, 5, and 9 are exhibited in Fig. 13. In addition, some evaluation criteria, such as the peak sidelobe ratio
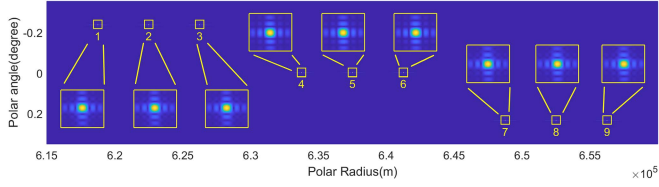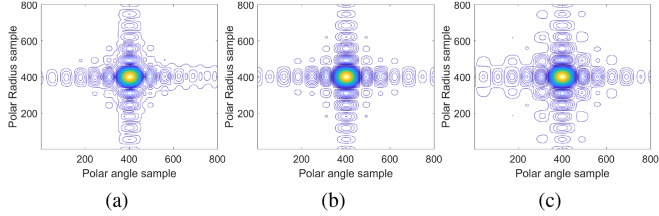
Fig. 12. 2-D imaging results of the point targets.

Fig. 13. Focusing results of point targets 1, 5, and 9.

TABLE II
EVALUATION CRITERIA OF FIG. 13

		Target 1	Target 5	Target 9
Range	PSLR	−13.51 dB	−13.53 dB	−13.69 dB
	ISLR	−9.42 dB	−9.37 dB	−9.50 dB
Azimuth	PSLR	−13.44 dB	−14.06 dB	−14.29 dB
	ISLR	−10.25 dB	−9.80 dB	−10.03 dB

(PSLR) and integrated sidelobe ratio (ISLR) of the radius and azimuth profile are demonstrated in Table II. These results show that the point scatters can focus well in different positions of the wide-swath image.

B. Ambiguity Suppression Effect

The ambiguity suppression simulations are performed on the point target and the line target, where the length of the line target is comparable to the pulse width. The Costas-DFC waveform [28] and the cross-correlation optimized NLFM waveform [13] have been applied as comparisons. The point target is placed at the scene center.

The ambiguity elimination results of the point target under the SSC-DFC waveform are shown in Fig. 14. Since the elevation DBF set notches at the ambiguous sources that generate the focused energy, the ambiguity suppression reaches 59.9 dB in the radius dimension. Owing to the same spectrum distribution of different SSC-DFC waveforms, the azimuth ambiguity reduces to −49.58 dB after the Doppler filtering. For the Costas-DFC waveform, the ambiguous energy smears within the range of two times the pulse width. Placing the DBF notch in the center of this range is insufficient for the smeared energy on both sides. The peak energy is −47.35 dB for the radius ambiguous position. The unfocused energy from different Costas-DFC waveforms cannot be removed by the azimuth filter, and the peak value of the ambiguity component raises to −34.6 dB. The range ambiguity of the NLFM waveform has benefited from the optimization of the CCE performance, and it has decreased by nearly 6 dB
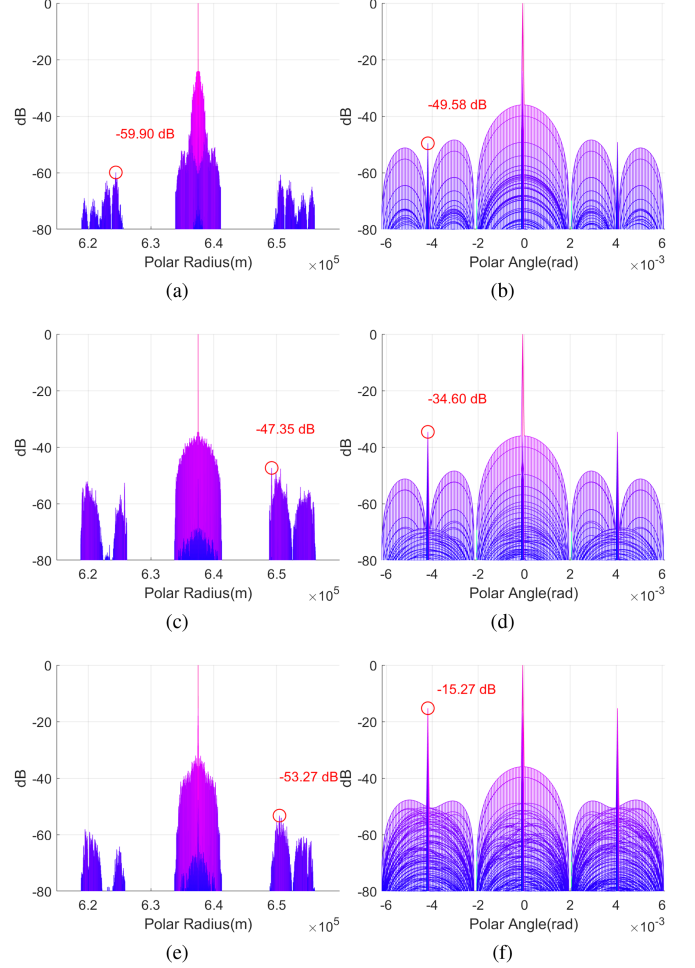

Fig. 14. Ambiguity suppression effect of point target. (a) Radius dimension view of the SSC-DFC. (b) Azimuth angel dimension view of the SSC-DFC. (c) Radius dimension view of the Costas-DFC. (d) Azimuth angel dimension view of the Costas-DFC. (e) Radius dimension view of the NLFM. (f) Azimuth angel dimension view of the NLFM.
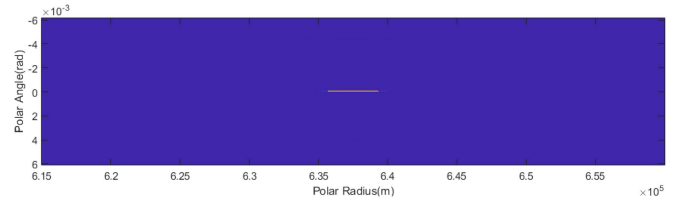

Fig. 15. Imaging results of the line target with SSC-DFC waveform.

compared to the Costas-DFC, which is −53.27 dB. But the azimuth ambiguity performance greatly deteriorates. The point target suppression is only 15.27 dB.

Considering the accumulation of the CCE when imaging a distributed scene with quasi-orthogonal waveforms, the following simulation is set to evaluate the ambiguity suppression performance of different waveforms for a line target placed in the center of the scene along the radius direction. Fig. 15 shows the line target image with a length of 2.88 Km, which is equivalent to the pulse width.
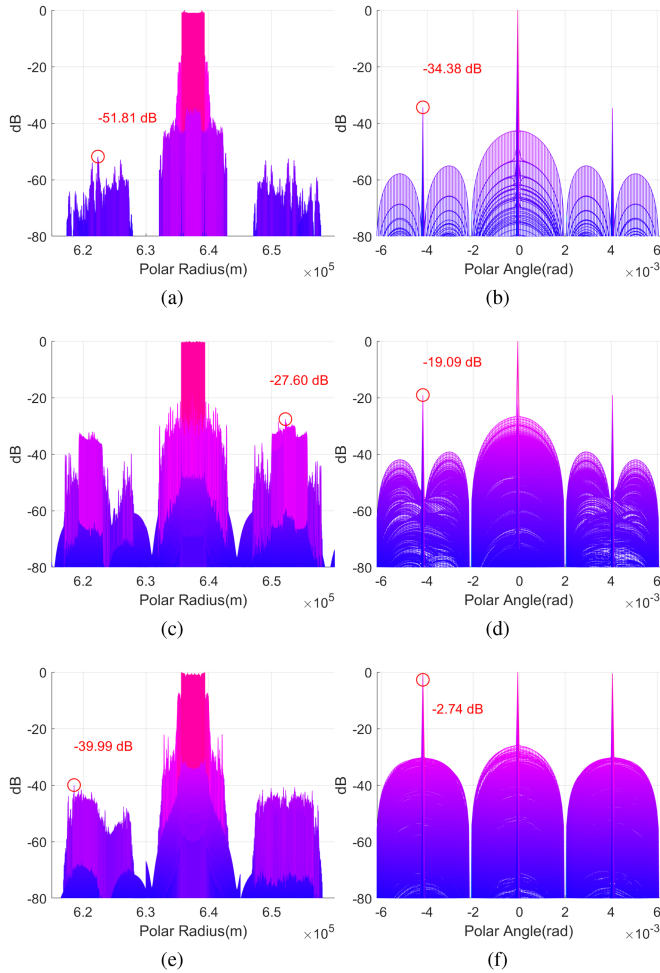
Fig. 16. Ambiguity suppression effect of line target. (a) Radius dimension view of the SSC-DFC. (b) Azimuth angel dimension view of the SSC-DFC. (c) Radius dimension view of the Costas-DFC. (d) Azimuth angel dimension view of the Costas-DFC. (e) Radius dimension view of the NLFM. (f) Azimuth angel dimension view of the NLFM.

Fig. 16 demonstrates the imaging results of the line target under different waveforms. In addition to the main lobe energy of the current scatter point, the energy at each range cell also contains the sidelobe from the scatter points nearby. Relying on the precise ambiguity positioning and suppression, the SSC-DFC waveform maintains a considerable range ambiguity resolving performance when dealing with a line target. Its azimuth ambiguity suppression is below 34 dB. Due to the insufficient suppression of the smeared ambiguity energy, the range ambiguity energy of the Costas-DFC waveform for the line target deteriorates by nearly 20 dB. Since the sidelobe energy of the different Costas-DFC cannot focus on the azimuth dimension, the azimuth ambiguity suppression is only 19.07 dB. The range ambiguity suppression of the NLFM is superior to the Costas-DFC. However, since more waveform energy scatters outside the main lobe, the match filtering outputs from the distributed scattering points are superimposed on each other, and azimuth filtering will almost fail. Table III lists the range ambiguity to signal ratio (RASR) and the azimuth ambiguity to

TABLE III
AMBIGUITY TO SIGNAL RATIO

		SSC-DFC	Costas-50	Costas-LFM
Point Target	RASR	–59.90 dB	–47.35 dB	–53.27 dB
	AASR	–49.58 dB	–34.60 dB	–15.27 dB
Line Target	RASR	–51.81 dB	–27.60 dB	–39.99 dB
	AASR	–34.38 dB	–19.09 dB	–2.74 dB

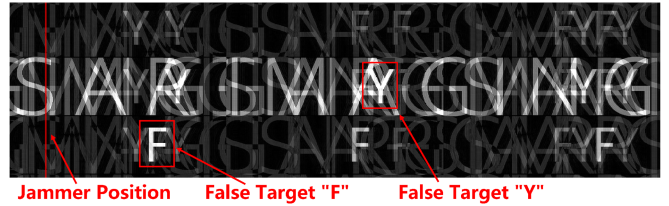Fig. 17. True target and false target in the wide-swath scene.

Fig. 18. Imaging without the elevation DBF.

signal ratio (AASR) results of the different waveforms for the point and line target imaging.

C. Jamming Suppression Effect

For clarity, a wide-swath scene shown in Fig. 17 was used to verify the anti-interference performance of the method proposed in this article. The jammer is located at 617.5 Km. The white letters represent the true targets, while the red letters are the false targets forwarded by the deception jammer. The jamming strategy includes forwarding in the current PRT and across the PRTs. F is the false target induced by the current PRT forwarding, which locates at the same subswath as the jammer. Y is forwarded in the subsequent PRTs, so it is located at the farther subswaths. Y overlaps the real targets.

Fig. 18 shows the SAR imaging without the elevation DBF. Similar to the relationship between the real targets and their ambiguous components, the false targets also exhibit the ambiguity distribution between the subswaths.

Since the range ambiguity component is the cross-correlation output of two SSC-DFC waveforms, the output peak phases will vary with the waveform combination. This mismatch between the slow time phase and the Doppler steering vector will cause the failure of the azimuth ambiguity resolution. So, there will be azimuth artifacts for the range ambiguous component, both for the real and false targets. It can be seen more clearly in Fig. 20.

If the DBF points to the current range cell and only suppresses the signal from the ambiguous sources, the range ambiguity resolving can be well achieved. However, the lack of constraints
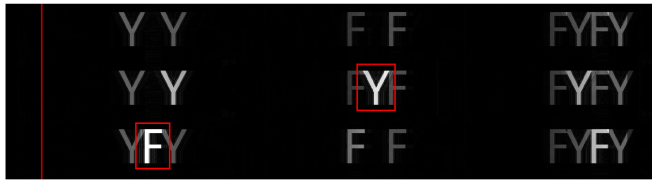
Fig. 19.   Imaging with the ambiguity suppression only.

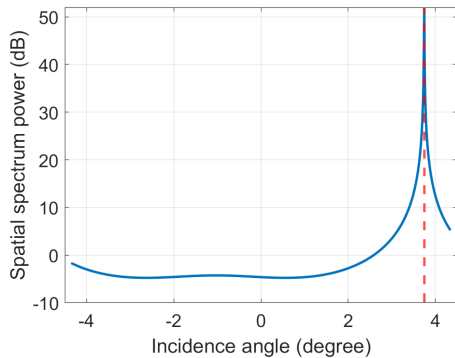Fig. 20.   False target image after the clutter cancellation.

Fig. 21.   Jammer finding by the spectrum estimation algorithm.
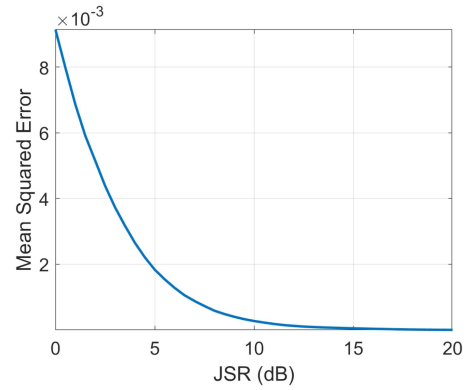

Fig. 22.   MSE against different JSR.

Fig. 23.   Interference suppression for the whole image.

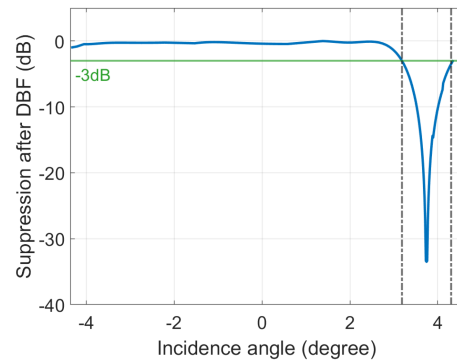

Fig. 24.   Interference suppression for the whole image.

Fig. 25.   Interference suppression for the whole image.

on the incoming wave from the jammer's direction leads to a certain suppression effect. The false targets introduced by the strong jamming signal still exist in the SAR image, as shown in Fig. 19.

Accurate jammer estimation is the prerequisite for jamming suppression. The false target image after the clutter cancellation is shown in Fig. 20. Clutter cancellation greatly enhances JSR. Only the false targets and their ambiguous components are visible in the image.

An appropriate threshold is set to mark the pixels covered by the false targets. The signals focused on these pixels have the same steering vector pointing to the jammer's location. Fig. 21 gives the direction of the jammer using the MUSIC spectrum estimation algorithm.

Considering that the JSR of the pixels used for angle estimation is relatively high, better angle estimation can be obtained according to the curve in Fig. 22.

After obtaining the accurate elevation angle of the jammer, precise jamming suppression can be achieved by adding a spatial notch at this angle. If the ambiguous and jamming components are spatially filtered in the entire image without marking the false target area, a dark stripe will appear at the jammer's location, resulting in the loss of imaging information near the jammer, as shown in Fig. 23.

Applying different spatial filters for the false target region and the other region can preserve the real scene information when performing the jamming suppression. Fig. 24 shows the intact HRSW image without the ambiguity and jamming.

Fig. 25 illustrates the impact of the DBF on the scatter, which locates at the same range cell with the false target. When the false target is far away from the jammer, the space filtering basically has no effect on the imaging result. Only when the false target
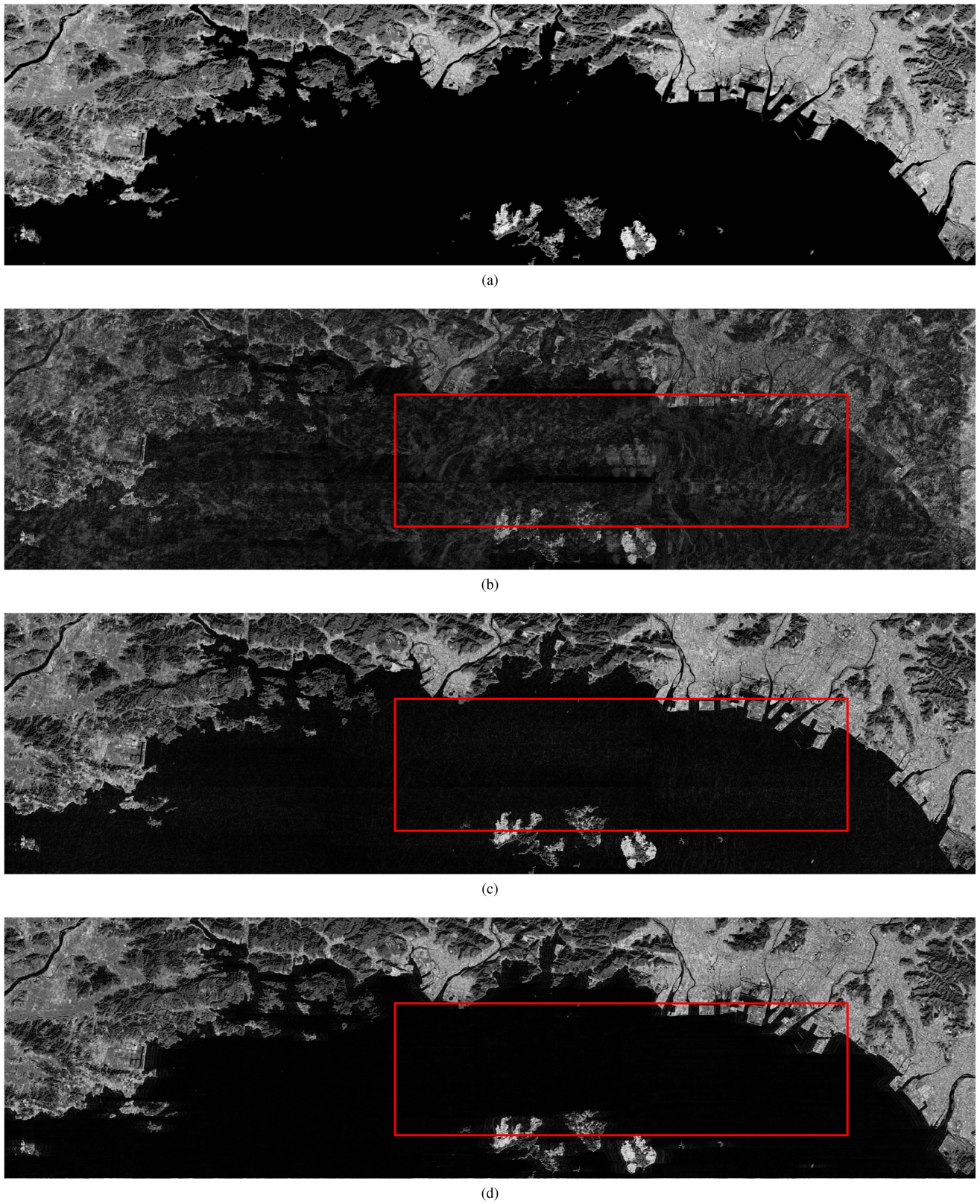
Fig. 26. Wide-swath imaging simulation on the real scene for waveform comparison. (a) Origin scene. (b) Wide-swath image by the NLFM. (c) Wide-swath image by the Costas-DFC. (b) Wide-swath image by the SSC-DFC.
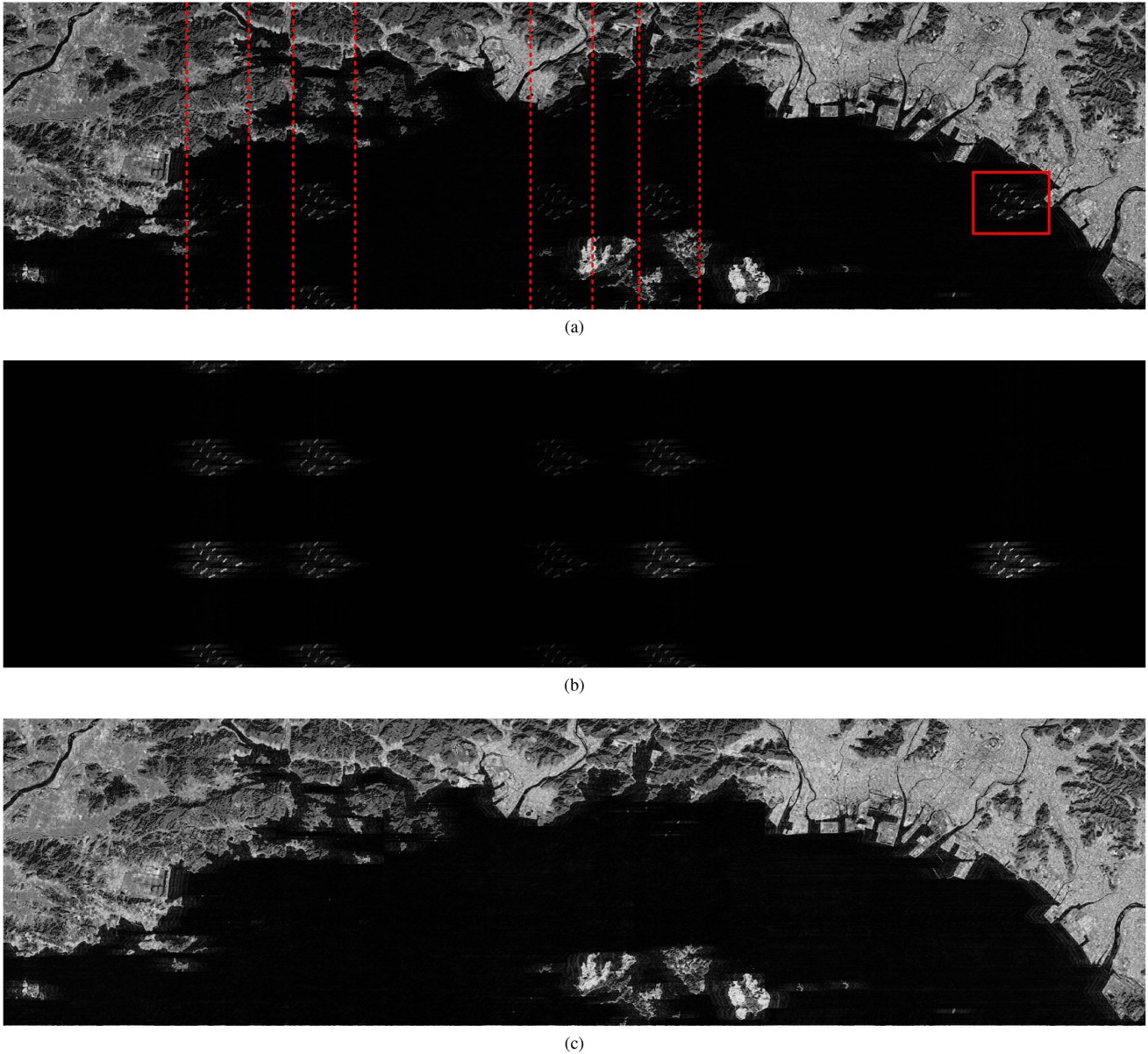
Fig. 27. Real scene simulation for anti-interference verification. (a) Real scene image with deceptive jamming. (b) False targets region. (c) Real scene image after the jamming suppression.

is located near the jammer, the steering vector of false target is close to that of the scene echo at that position. In this case, suppression of the false target will degrade the real scene echo energy. When there are false targets near the jammer, the 3 dB angular width of the energy loss is about $1.12°$.

D. Distributed Target Simulation

At last, a sea scene near Himeji City has been simulated to verify the effectiveness of the proposed method, The full images obtained by using different waveforms are shown in Fig. 26. Fig. 26(a) is the original scene provided as the input of the simulation. Although the orthogonal NLFM optimizes the range ambiguity suppression performance, its azimuth ambiguity solution ability is so poor that the images of different

azimuth regions almost overlap in the final wide-swath image in Fig. 26(b). The image based on the Costas-DFC waveform can achieve the two-dimensional ambiguity resolution, as shown in Fig. 26(c). However, in the part of the sea image within the red rectangle frame, the presence of ambiguous components can also be observed. The same region of the SSC-DFC image has better imaging quality. Here, structural similarity (SSIM) [32] is applied to evaluate the image quality. The original scene is calculated as the benchmark. A larger value means that the SAR image is closer to the original scene. The SSC-DFC waveform result in Table IV further verified its superior wide-swath imaging quality.

In the antijamming simulation shown in Fig. 27, multiple false targets in the red frame are formed by the deception jamming. The ambiguous components of the false targets are visible in

TABLE IV
COMPARISON OF THE IMAGE QUALITY USING SSIM

Waveform	NLFM	Costas-DFC	SSC-DFC
SSIM of the full image	0.6803	0.9045	0.9543
SSIM in the red frame	0.5379	0.8588	0.9733

the corresponding regions bound by the dashed lines. After the interference suppression, the false targets and their ambiguous components are removed successfully, and the complete wide-swath scene is preserved.

V. CONCLUSION

Range ambiguity resolving and deception jamming suppression are challenging technical problems for the HRWS SAR. In this article, a new approach integrating agile waveform and elevation DBF is proposed to solve the abovementioned problems simultaneously. The distributed imaging priority is hard to be obtained by the orthogonal waveforms, which share the same spectrum. As an agile waveform, the cyclic shift characteristics between the SSC-DFC waveforms make it have extremely low azimuth residual and focused range ambiguity energy that is conducive to DBF processing. The false target area extraction after the clutter cancellation can not only realize the angle estimation of the jammer but also allow the signal from the jammer to be filtered only in the false target area. Based on the accurate ambiguity position and the jammer estimation result, the range ambiguity resolving and jamming suppression under the HRWS SAR can be realized simultaneously by the subarea DBF. The effectiveness of this scheme has been validated by various simulated data results.

REFERENCES

[1] G. Xu, B. Zhang, J. Chen, and W. Hong, "Structured low-rank and sparse method for ISAR imaging with 2-D compressive sampling," *IEEE Trans. Geosci. Remote Sens.*, vol. 60, pp. 1–14, Nov. 2022.
[2] G. Xu, B. Zhang, H. Yu, J. Chen, M. Xing, and W. Hong, "Sparse synthetic aperture radar imaging from compressed sensing and machine learning: Theories, applications, and trends," *IEEE Geosci. Remote Sens. Mag.*, vol. 10, no. 4, pp. 32–69, Dec. 2022.
[3] G. Xu, B. Zhang, J. Chen, F. Wu, J. Sheng, and W. Hong, "Sparse inverse synthetic aperture radar imaging using structured low-rank method," *IEEE Trans. Geosci. Remote Sens.*, vol. 60, pp. 1–12, Oct. 2021.
[4] J. C. Curlander and R. N. McDonough, *Synthetic Aperture Radar: Systems and Signal Processing*. Hoboken, NJ, USA:Wiley, 1991.
[5] M. Alshaya, M. Yaghoobi, and B. Mulgrew, "High-resolution wide-swath IRCI-free MIMO SAR," *IEEE Trans. Geosci. Remote Sens.*, vol. 58, no. 1, pp. 713–725, Jan. 2020.
[6] X. Chang, Y. Li, and Y. Zhao, "An improved scattered wave deceptive jamming method based on a moving jammer beam footprint against a three-channel short-time SAR GMTI," *IEEE Sensors J.*, vol. 21, no. 4, pp. 4488–4499, Feb. 2021.
[7] B. Zhao, L. Huang, J. Li, M. Liu, and J. Wang, "Deceptive SAR jamming based on 1-bit sampling and time-varying thresholds," *IEEE J. Sel. Topics Appl. Earth Observ. Remote Sens.*, vol. 11, no. 3, pp. 939–950, Mar. 2018.
[8] Z.-F. Wu, H.-P. Xu, J.-W. Li, and W. Liu, "Research of 3-D deceptive interfering method for single-pass spaceborne InSAR," *IEEE Trans. Aerosp. Electron. Syst.*, vol. 51, no. 4, pp. 2834–2846, Oct. 2015.
[9] W.-Q. Wang, "Mitigating range ambiguities in high-PRF SAR with OFDM waveform diversity," *IEEE Geosci. Remote Sens. Lett.*, vol. 10, no. 1, pp. 101–105, Jan. 2013.
[10] J.-H. Kim, M. Younis, A. Moreira, and W. Wiesbeck, "A novel OFDM chirp waveform scheme for use of multiple transmitters in SAR," *IEEE Geosci. Remote Sens. Lett.*, vol. 10, no. 3, pp. 568–572, May 2013.
[11] G. Krieger, "MIMO-SAR: Opportunities and pitfalls," *IEEE Trans. Geosci. Remote Sens.*, vol. 52, no. 5, pp. 2628–2645, May 2014.
[12] F. Bordoni, G. Krieger, and M. Younis, "Multifrequency subpulse SAR: Exploiting chirp bandwidth for an increased coverage," *IEEE Geosci. Remote Sens. Lett.*, vol. 16, no. 1, pp. 40–44, Jan. 2019.
[13] G. Jin et al., "Mitigating range ambiguities with advanced nonlinear frequency modulation waveform," *IEEE Geosci. Remote Sens. Lett.*, vol. 16, no. 8, pp. 1230–1234, Aug. 2019.
[14] N. Ustalli and M. Villano, "High-resolution wide-swath ambiguous synthetic aperture radar modes for ship monitoring," *Remote Sens.*, vol. 14, no. 13, 2022, Art. no. 3102.
[15] M. Lou et al., "Low probability of intercept waveform optimization method for SAR imaging," in *Proc. IEEE Int. Geosci. Remote Sens. Symp.*, 2021, pp. 3963–3966.
[16] K.-W. Lee and W.-K. Lee, "Waveform diversity for SAR ECCM based on random phase and code rate transition," *Int. J. Microw. Wireless Technol.*, vol. 9, no. 6, pp. 1345–1354, 2017.
[17] Z. Tang, Y. Deng, H. Zheng, and R. Wang, "High-fidelity SAR intermittent sampling deceptive jamming suppression using azimuth phase coding," *IEEE Geosci. Remote Sens. Lett.*, vol. 18, no. 3, pp. 489–493, Mar. 2021.
[18] G. Nie, G. Liao, C. Zeng, X. Zhang, and D. Li, "Joint radio frequency interference and deceptive jamming suppression method for single-channel SAR via sub-pulse coding," *IEEE J. Sel. Topics Appl. Earth Observ. Remote Sens.*, vol. 16, pp. 787–798, Dec. 2022.
[19] B. Zhao, L. Huang, J. Li, and P. Zhang, "Target reconstruction from deceptively jammed single-channel SAR," *IEEE Trans. Geosci. Remote Sens.*, vol. 56, no. 1, pp. 152–167, Jan. 2018.
[20] B. Zhao, L. Huang, and W. Sun, "Target reconstruction in deceptively jammed SAR via ADMM," *IEEE Sensors J.*, vol. 19, no. 11, pp. 4331–4339, Jun. 2019.
[21] K. Zhou, D. Li, F. He, S. Quan, and Y. Su, "A sparse imaging method for frequency agile SAR," *IEEE Trans. Geosci. Remote Sens.*, vol. 60, pp. 1–16, Feb. 2022.
[22] W. Xiong, G. Zhang, F. Wen, Y. Zhang, and J. Yin, "Trilinear decomposition-based spatial-polarisational filter method for deception jamming suppression of radar," *IET Radar, Sonar Navigation*, vol. 10, no. 4, pp. 765–773, 2016.
[23] G. Rongbing, W. Jianguo, and H. Chuan, "Rebound jamming suppression by two-channel SAR," *Signal Process.*, vol. 21, no. 1, pp. 27–30, 2005.
[24] X.-Y. Ma, J.-M. Qin, Z.-H. He, J. Yang, and Q.-H. Lu, "Three-channel cancellation of SAR blanketing jamming suppression," *ACTA Electonica Sinica*, vol. 35, no. 6, 2007, Art. no. 1015.
[25] S. Cheng et al., "A joint azimuth multichannel cancellation (JAMC) antibarrage jamming scheme for spaceborne SAR," *IEEE J. Sel. Topics Appl. Earth Observ. Remote Sens.*, vol. 15, pp. 9913–9926, Nov. 2022.
[26] B. Correll, J. K. Beard, and C. N. Swanson, "Costas array waveforms for closely spaced target detection," *IEEE Trans. Aerosp. Electron. Syst.*, vol. 56, no. 2, pp. 1045–1076, Apr. 2020.
[27] J. P. Costas, "A study of a class of detection waveforms having nearly ideal range–Doppler ambiguity properties," *Proc. IEEE*, vol. 72, no. 8, pp. 996–1009, Aug. 1984.
[28] G. Dai, L. Zhang, and S. Huan, "Costas DFC-based random stepped widebandwaveform for interference countermeasure in SAR imagery," *Sensors*, vol. 22, no. 9, 2022, Art. no. 3197.
[29] F. Bordoni, M. Younis, and G. Krieger, "Performance investigation on the high-resolution wide-swath SAR system operating in multisubpulse mode," in *Proc. IEEE Int. Geosci. Remote Sens. Symp.*, 2012, pp. 3568–3571.
[30] G. Dai, L. Zhang, S. Huan, and Z. Wang, "Random stepped-frequency SAR imagery with full cell doppler coherent processing," *IEEE Geosci. Remote Sens. Lett.*, vol. 19, pp. 1–5, Feb. 2021.
[31] F. Brigui, L. Thirion-Lefevre, G. Ginolhac, and P. Forster, "New SAR algorithm based on orthogonal projections for MMT detection and interference reduction," *IEEE Trans. Geosci. Remote Sens.*, vol. 52, no. 7, pp. 3800–3811, Jul. 2014.
[32] Z. Wang, A. C. Bovik, H. R. Sheikh, and E. P. Simoncelli, "Image quality assessment: From error visibility to structural similarity," *IEEE Trans. Image Process.*, vol. 13, no. 4, pp. 600–612, Apr. 2004.

GanE Dai was born in Zhejiang, China, in 1987. He received the B.S. degree in information countermeasure technology and the M.S. degree in signal and information processing from Xidian University, Xi'an, China, in 2009 and 2011, respectively. He is currently working toward the Ph.D. degree in signal and information processing with the School of Electronics and Communication Engineering, Sun Yat-sen University, Shenzhen, China.

His research interests include radar imaging and radar signal processing.

Lei Zhang (Member, IEEE) was born in Zhejiang, China, in 1984. He received the Ph.D. degree in signal and information processing from Xidian University, Xi'an, China, in 2012.

He is an Associate Professor with the School of Electronics and Communication Engineering, Sun Yat-sen University, Shenzhen, China. His research interests include radar imaging [synthetic aperture radar (SAR)/inversed SAR (ISAR)] and motion compensation.

Sha Huan received the B.Eng. degree in information engineering and the Ph.D. degree in electromagnetic field and microwave technique from the Beijing Institute of Technology, Beijing, China, in 2006 and 2012, respectively.

From 2012 to 2017, she was a Senior Engineer with the Beijing Institute of Radio Measurement, Beijing, China. In 2017, she joined Guangzhou University, Guangzhou, China, as a Lecturer. Her research interests include high-resolution radar imaging and radar antijamming processing.